



# Plastic Deformation Behavior of 40Fe–25Ni–15Cr–10Co–10V High-Entropy Alloy for Cryogenic Applications

Min Ji Jang<sup>1</sup> · Hyunjeong Kwak<sup>1</sup> · Ye Won Lee<sup>1</sup> · Youjin Jeong<sup>1</sup> · Jahong Choi<sup>2</sup> · Yong Hee Jo<sup>1</sup> · Won-Mi Choi<sup>1</sup> · Hyun Je Sung<sup>3</sup> · Eun Yoo Yoon<sup>4</sup> · S. Praveen<sup>1</sup> · Sunghak Lee<sup>1</sup> · Byeong-Joo Lee<sup>1</sup> · Mohamed Ibrahim Abd El Aal<sup>5,6</sup> · Hyoung Seop Kim<sup>1</sup>

Received: 30 July 2018 / Accepted: 21 August 2018 / Published online: 1 September 2018  
© The Korean Institute of Metals and Materials 2018

## Abstract

A single FCC phase 40Fe–25Ni–15Cr–10Co–10V high-entropy alloy was designed, fabricated, and evaluated for potential cryogenic applications. The alloy forms a single FCC phase and exhibits higher yield strength, tensile strength, and elongation at cryogenic temperature (77 K) than at room temperature (298 K). The superior tensile properties at cryogenic temperature are discussed based on the formation of deformation twins during the tensile test at cryogenic temperature. In addition, a constitutive model reflecting the cryogenic deformation mechanism (i.e., twinning-induced plasticity) was implemented into the finite element method to analyze this behavior. Experimental results and the finite element analysis suggest that the increase in plastic deformation capacity at cryogenic temperature contributes to the formation of deformation twins.

**Keywords** High-entropy alloy · Deformation twinning · Cryogenic deformation · Plastic deformation behavior · Finite element analysis

## 1 Introduction

There is a growing demand for energy resources with the rapid advancement in technology. There are numerous types of energy resources which are yet to be discovered in the Arctic ocean [1]. The exploration of these energy resources

from the Arctic ocean is a challenging task due to harsh conditions of the Arctic ocean. In addition, the storage and transportation of natural gas have to be carried out at a cryogenic temperature due to its low energy density. The shipping distance of natural gas can be shortened by thousands of kilometers when operating the Arctic route compared to existing routes [2]. This will lead to a reduction in fuel consumption and exhaust gas, resulting in lower operating costs and eco-friendly effect. Thus, the development of advanced material with superior properties under extreme conditions are of great importance for ice breakers (specially constructed shipping vessels), offshore plants, liquid nitrogen carriers and pipelines, and for a sustained presence in the polar regions.

In general, the face-centered cubic (FCC) crystal structure materials, such as AISI 300 series stainless steel, aluminum alloy, and nickel steel, are most widely used as cryogenic materials for ships and offshore structures [3] due to their enhanced mechanical properties at low temperatures [3, 4]. This is also the case with recently studied high-entropy alloys (HEAs) which possess excellent mechanical properties at cryogenic temperature. Gludovatz et al. [5] have demonstrated an increase in yield strength, ultimate tensile strength, and fracture strain with excellent fracture

✉ Hyoung Seop Kim  
hskim@postech.ac.kr

<sup>1</sup> Department of Materials Science and Engineering, Pohang University of Science and Technology (POSTECH), Pohang 37673, Republic of Korea

<sup>2</sup> Department of Mechanical Engineering, Pohang University of Science and Technology (POSTECH), Pohang 37673, Republic of Korea

<sup>3</sup> Technical Research Laboratories, POSCO, Pohang 37859, Republic of Korea

<sup>4</sup> Materials Deformation Department, Korea Institute of Materials Science, Changwon 51508, Republic of Korea

<sup>5</sup> Mechanical Engineering Department, Prince Sattam Bin Abdulaziz University, Wadi Addawasir, Kingdom of Saudi Arabia

<sup>6</sup> Mechanical Design and Production Department, Zagazig University, Zagazig 44519, Egypt

toughness at cryogenic temperature. In addition, HEAs are known to have high strength, strength retention at higher temperatures, better thermal stability, and good corrosion resistance [5–13]. Recently, Kang et al. [14] successfully demonstrated the manufacturing of several kilograms of HEA, indicating the possibility of commercialization in the future.

In this study, an HEA suitable for cryogenic environments was designed and its suitability as a material for cryogenic environments was evaluated through mechanical tests and microstructural analyses. In alloy design for cryogenic environments, it is important to study the mechanical properties of the alloys and the shape design considering the microstructural changes during plastic deformation. For this purpose, this study included the theoretical description of the deformation behavior of the HEA at room temperature and cryogenic temperature using constitutive equations for finite element analyses.

## 2 Materials and Methods

### 2.1 Experimental Methods

Phase equilibrium thermodynamic modeling was employed to design a 40Fe–25Ni–15Cr–10Co–10V HEA with a single FCC phase over a wide range of temperature. The thermodynamic database TCFE2000 and its upgraded version [15, 16] were used for phase diagram calculations [17, 18]. The designed alloy was fabricated using vacuum induction melting of pure elements (purity 99% or more). The ingot was homogenized in an argon atmosphere at 1100 °C for 6 h, followed by water quenching. The initial thickness of the homogenized slab was 8 mm, and it was cold rolled to a final thickness of ~1.5 mm (~80% thickness reduction). The rolled plate was annealed at 900 °C for 10 min in an argon atmosphere, followed by water quenching. The secondary processing of as-cast alloy is schematically illustrated in Fig. 1.

Rectangular dog-bone shaped tensile specimens were made with the loading direction parallel to the rolling direction. The tensile tests were carried out using an electromechanical testing machine (Instron 1361, USA) at room and cryogenic temperatures and at a constant strain rate of  $10^{-3} \text{ s}^{-1}$ . Vickers hardness measurements were conducted at a regular spatial interval from the middle to the edge of the gage (HM-220, MITUTOYO, Japan).

The X-ray diffraction (XRD) analysis was performed to identify the crystal structure of the designed alloy. The surface perpendicular to the normal direction of the specimen was mechanically polished with silicon carbide papers of 400, 600, 800, and 1200 grit, followed by diamond suspensions of 3, 1, and 0.5  $\mu\text{m}$ . Final polishing was done with a mixture of 50% ethanol and 50% colloidal silica to obtain a mirror-like surface. The polished specimens were checked for twin formation using electron backscatter diffraction (EBSD) analysis. The EBSD data was analyzed using the commercial software (TSL OIM Analysis 7).

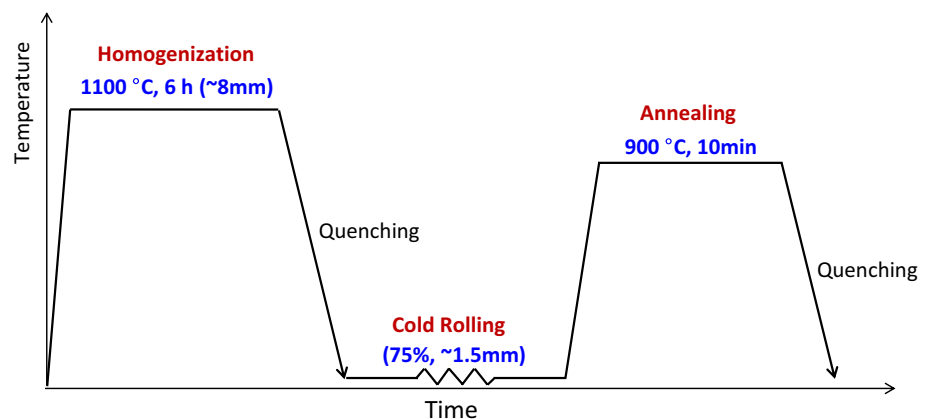
The finite element method (FEM) associated with a constitutive model (based on a model reflecting twinning-induced plasticity) was utilized to simulate the plastic deformation behavior of the alloy. In order to use FEM, a user subroutine UMAT in the commercial program ABAQUS was constructed and implemented.

### 2.2 Constitutive Model

The constitutive equations used in the present work to model the deformation behavior of the alloy are as follows [19]. The evolution of dislocation density ( $\rho$ ) due to shear strain ( $\gamma_g$ ) associated with the dislocation glide is described in the Kocks–Mecking–Estrin equation [20, 21]:

$$\frac{d\rho}{d\gamma_g} = \frac{1}{bL} + \frac{k}{b} \sqrt{\rho} - f\rho \quad (1)$$

**Fig. 1** Schematic of secondary processing of as cast 40Fe–25Ni–15Cr–10Co–10V high entropy alloy



where  $b$  is the magnitude of the Burgers vector,  $k$  is coefficient relating to a thermal storage, and  $f$  denotes the dynamic recovery coefficient. The first term on the right-hand side is related to the accumulation of dislocations at the obstacles with spacing  $L$  (for example, grain boundary and/or twin boundary). The second term refers to the dislocation storage at the obstacles related to the dislocation (e.g., dislocation cell walls). The last term is related to the dynamic recovery by dislocation annihilation.

The spacing of obstacles is given by [22, 23]

$$\frac{1}{L} = \frac{1}{d} + \frac{1}{t} \tag{2}$$

where  $d$  is the average grain size and  $t$  is the mean twin spacing. According to Bouaziz et al. [22, 23], quantity  $t$  has the following relationship with average twin thickness  $e$  and twin volume fraction  $F$ :

$$t = 2e \cdot \frac{1 - F}{F} \tag{3}$$

The evolution of twin volume fraction  $F$  above the twinning onset strain  $\epsilon_0$  can be expressed as follows [19]:

$$F = F_0 + (F_\infty - F_0) \times \operatorname{erf}\left(\frac{\epsilon - \epsilon_0}{\tilde{\epsilon}}\right) \tag{4}$$

where  $F_0$  is the initial twin volume fraction at  $\epsilon = \epsilon_0$ ,  $F_\infty$  is the saturated value of the twin volume fraction, and  $\tilde{\epsilon}$  is the parameter that governs the rate of evolution.

The plastic shear strain increment consists of contributions from dislocation glide and twinning [22, 23], and it can be expressed as follows:

$$d\gamma = (1 - F) \cdot d\gamma_g + \gamma_t \cdot dF \tag{5}$$

where  $\gamma_t$  is the twinning shear strain which is equal to  $1/\sqrt{2}$  [22, 23]. The first term on the right-hand side is related to the dislocation glide, and the second term represents twinning.

The relationship between flow stress ( $\sigma$ ) and dislocation density ( $\rho$ ) is calculated using the following Taylor equation [24]:

$$\sigma = \sigma_0 + \alpha M G b \sqrt{\rho} \tag{6}$$

where  $\sigma_0$  is the friction stress needed to activate the dislocation glide,  $\alpha$  is a numerical constant,  $M$  is the Taylor factor accounting for texture, and  $G$  is the shear modulus.

### 3 Results and Discussion

#### 3.1 Alloy Design and Fabrication

In order to design a suitable alloy for the present work, three factors were considered: cost competitiveness, corrosion resistance, and stability of the FCC single phase. To increase

the price competitiveness, the alloy is designed with high Fe content and low Co content. To stabilize the austenitic phase and enhance the low-temperature toughness, Ni was added to the alloy [25–27]. To have a better corrosion resistance, the Cr content with more than 15% was considered for the alloy design. Based on the binary phase diagrams, V with other elements exists as a single-FCC phase over a wide range of temperature [25]. In addition, its atomic size is larger than most other elements which can enhance the solid solution strengthening effect [25]. Based on the above-mentioned points, an alloy system based on Fe–Ni–Cr–Co–V was selected for thermodynamic calculations. Finally, an alloy that would possess a single FCC phase over a wide range of temperature was selected by calculation of thermodynamic states.

Consequently, the alloy with the composition of 40Fe–25Ni–15Cr–10Co–10V was designed for the present work, and the phase diagram of this alloy is shown in Fig. 2. It can be seen that the designed alloy has a single FCC phase over a wide temperature range (726–1346 °C). The heat treatment temperatures for homogenization (1100 °C) and annealing (900 °C) were chosen in this temperature range to get a single FCC phase. Figure 3 shows the XRD pattern of the sample in the annealed condition. It can be seen that a single FCC phase was formed, which agrees well with the calculated phase diagram.

#### 3.2 Deformation Behavior and Mechanical Properties

The plastic deformation behavior of the alloy at room and cryogenic temperatures are shown in Fig. 4, and the mechanical properties are summarized in Table 1. The yield strength, ultimate tensile strength, and the fracture

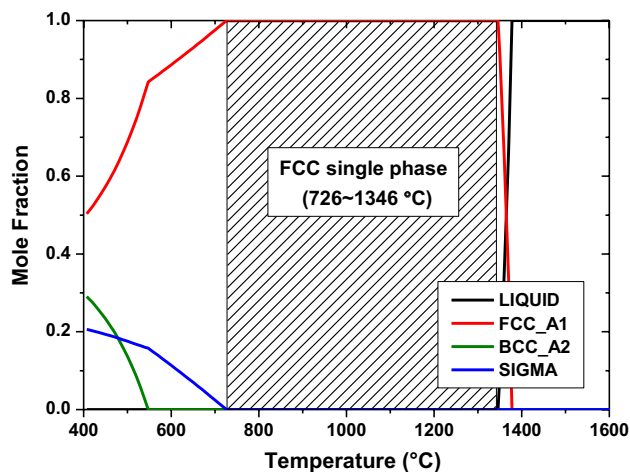


Fig. 2 Mole fractions of equilibrium phases in 40Fe–25Ni–15Cr–10Co–10V alloy in the temperature range 400–1600 °C

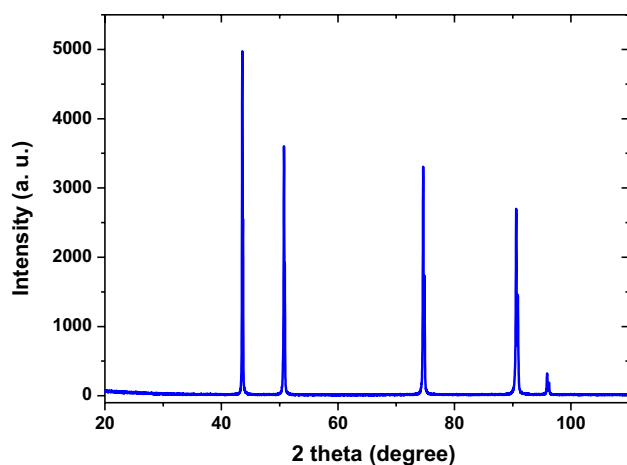


Fig. 3 XRD pattern of the alloy in annealed condition

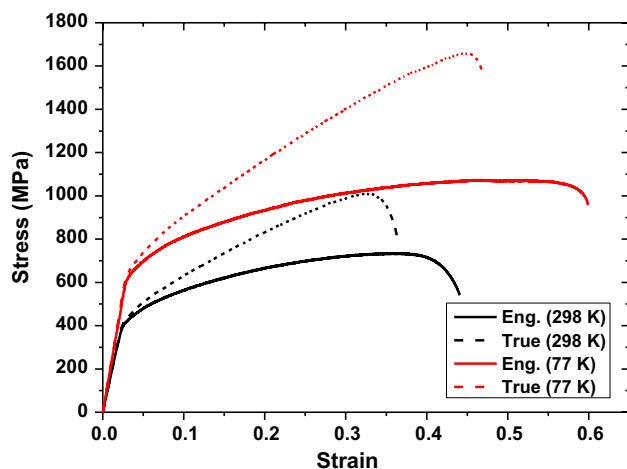


Fig. 4 Stress–strain curves of 40Fe–25Ni–15Cr–10Co–10V alloy at room and cryogenic temperature

**Table 1** Summary of mechanical properties of 40Fe–25Ni–15Cr–10Co–10 V alloy at room and cryogenic temperatures

	YS (MPa)	UTS (MPa)	Fracture strain (%)
RT (298 K)	393.20	735.61	44.08
CT (77 K)	612.64	1073.97	59.90

strain at cryogenic temperature increased by 55.8%, 46.0%, and 35.9%, respectively, as compared to the room temperature mechanical properties. This clearly implies that the mechanical properties of the alloy were enhanced significantly at cryogenic temperature.

### 3.3 Microstructure Analysis and Fractography

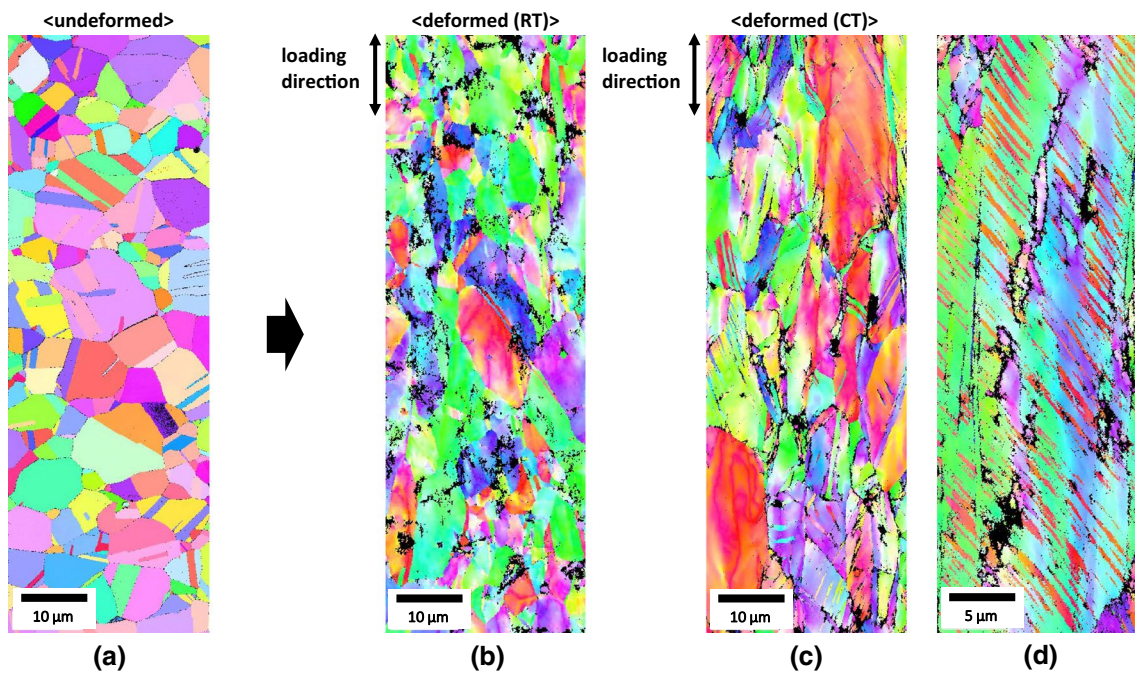
Figure 5 shows the EBSD inverse pole figure (IPF) map of the initial (un-deformed) and deformed (at room temperature and cryogenic temperature) specimens. The initial microstructure consists of equiaxed grains with profuse annealing twins (Fig. 5a). The estimated average grain size is approximately 8.8  $\mu\text{m}$  (excluding twin boundaries). After room temperature deformation (Fig. 5b), the microstructure along the direction of deformation consists of elongated grains. In the cryogenic deformed sample, the microstructure consists of deformation twinning with  $\Sigma 3$  twin boundaries ( $60^\circ \langle 111 \rangle$ ) and elongated grains (Fig. 5c, d). This implies that the dislocation glide acts as a primary deformation mechanism at room temperature, whereas deformation twinning act as an additional deformation mechanism at cryogenic temperature. The presence of twin boundaries can interfere with the dislocation movement and it may lead to an increased hardening capacity at cryogenic temperature [28]. Thus, the formation of deformation twins can be attributed to the excellent mechanical properties achieved at cryogenic temperature.

Figure 6 shows the SEM fractography of the deformed (at room temperature and cryogenic temperature) specimens. The microstructure with a high density of dimple structures can be observed on the tensile-fractured surfaces of both the specimens. The dimple structure indicates the micro-void coalescence which is a clear evidence of ductile fracture. The dimples on the cryogenic-fractured surface have finer feature compared with that on the fractured surface at room temperature. It is due to the further refining of microstructure at cryogenic temperature with the twin-activated deformation, which can be confirmed by comparison of Fig. 5b, c. Therefore, it is confirmed that the ductile fracture has occurred during the tensile deformation at both room temperature and cryogenic temperature, and that the cryogenic-deformed specimen has finer microstructure due to the formation of twin boundaries. The analysis of the fracture morphology is in good agreement with the corresponding stress–strain curves (Fig. 4).

### 3.4 Constitutive Model and Finite Element Analysis

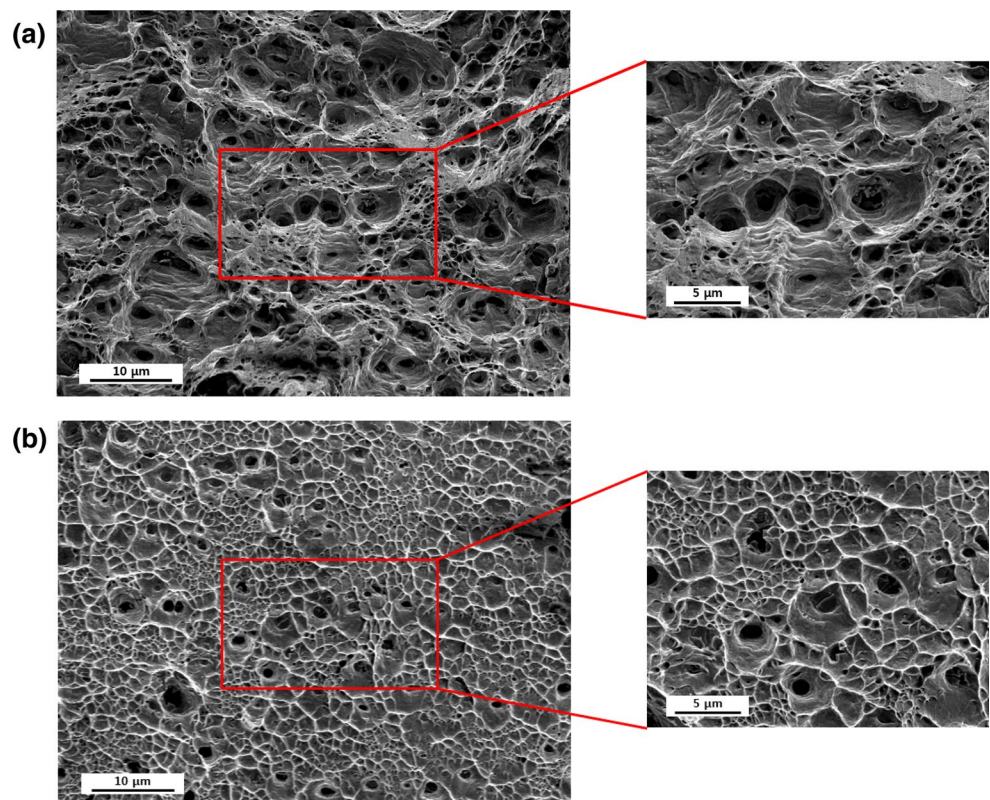
The plastic deformation behavior of the HEA can be described using the aforementioned set of equations. Some parameters in the model equations were fixed:  $\alpha = 0.33$ ,  $M = 3.06$ ,  $G = 81.2 \text{ GPa}$ ,  $b = 0.254 \text{ nm}$ ,  $d = 8.8 \mu\text{m}$ ,  $e = 0.01 \mu\text{m}$  [29], and  $F_0 = 0$ . The remaining constants were obtained from the experimental results and via a genetic algorithm for parameter identification. The constants obtained in this way are:  $\sigma_0 = 324 \text{ MPa}$ ,  $F_\infty = 0$ ,  $k = 0.02$ , and  $f = 2$  (for room temperature); and  $\sigma_0 = 546 \text{ MPa}$ ,  $F_\infty = 0.013$ ,  $\varepsilon_0 = 0.075$ ,  $\tilde{\varepsilon} = 0.3$ ,  $k = 0.024$ , and  $f = 1.94$  (for cryogenic temperature). By comparing the constant ( $F_\infty$ )





**Fig. 5** IPF maps **a** before deformation, **b** after deformation at room temperature, and **c, d** after deformation at cryogenic temperature

**Fig. 6** SEM fractography of specimens deformed **a** at room temperature and **b** at cryogenic temperature



at each temperature, it can be speculated that twinning is difficult to occur at room temperature. The  $k$  value reflects the efficiency of the dislocation structure that accumulates

the dislocations. Therefore, the accumulation of dislocations by the dislocation structure occurs more effectively at cryogenic temperature than at room temperature. In

addition, it can be seen that dynamic recovery was more active at room temperature than at cryogenic temperature by comparing the dynamic recovery coefficient,  $f$ . Based on the reported values of  $k$  (0.011) and  $f$  (3) for 304L steel and high Mn steel [22], it is clear that the dislocation storage mechanism is more efficient in the alloy of the present study. The dynamic recovery rate is slower in HEA, presumably due to the lattice distortion effect in HEAs [30, 31].

Figure 7a shows the deformation behaviors of HEA described using the above constants and the experimental stress–strain curves at room temperature and cryogenic temperature. The figure shows that the stress–strain curve obtained through the simulation (solid line) agrees well with the experimental stress–strain curve (symbol). The strain-hardening rate with respect to plastic strain is shown in Fig. 7b. It is clearly seen that the strain-hardening rate curves at room temperature and cryogenic temperature are different. The strain-hardening rate at room temperature decreases continuously till fracture, whereas the strain hardening rate at cryogenic temperature decreases continuously till true plastic strain of 0.075 and remain constant till true plastic strain of 0.12 and then starts decreasing with further deformation.

In general, when a plastic deformation is initiated in the metallic materials, the dislocation movement is hindered by a sharp increase in the dislocation density. This phenomenon is known as work hardening, and the work hardening rate will decrease due to the rearrangement of dislocations with further plastic deformation. However, when the deformation twins are generated by plastic deformation, the twin boundaries interfere with the dislocation glide and cause increased work hardening capacity. This leads to constant or improved work hardening rate [32, 33]. On further straining, the hardening rate steadily decreases due to less active deformation twinning.

In the case of HEA analyzed in this study, the deformation twinning starts to occur at  $\sim 0.075$  true plastic strain (twinning onset) during the cryogenic tensile test. The onset of twinning led to enhanced strain hardening capacity as compared to the room temperature strain hardening capacity. This is clearly reproduced in the simulations (red solid line in Fig. 7b). The volume fraction of twins in Fig. 5c was measured and compared with that predicted by Eq. (4). The experimental value is 0.0114 which matches with the theoretical value of 0.0105. The experimental results confirm that the model used in the present study is suitable for the description of microstructural changes due to plastic deformation and also for the change in deformation behaviors at room and cryogenic temperatures.

The tensile simulation results are shown in Fig. 8. The effective stress, plastic strain, and dislocation density are concentrated in the central region of the gage and have higher values at cryogenic temperature than at room temperature. The simulation indicates the twinning does not occur at room temperature, whereas it does occur at cryogenic temperature with the twin volume fraction being high at the central region of the gage.

In order to compare the stress distribution obtained from the simulation with those of the experimental results, the effective stress values were plotted along the tensile direction from the center of the gage for the sample deformed at room temperature (Fig. 9a). The Vickers hardness values measured along the gage of the room temperature deformed sample were multiplied by 3.3 and compared with the simulated values of effective stress. The correlation of tensile strength with hardness is also reported by Pavlina et al. [34]. Figure 9b shows the part where data has obtained and effective stress distribution. It is confirmed that the stress distribution of the specimen obtained through the simulation (black solid line) is in good agreement with the values obtained through the experiment (red symbol). We believe

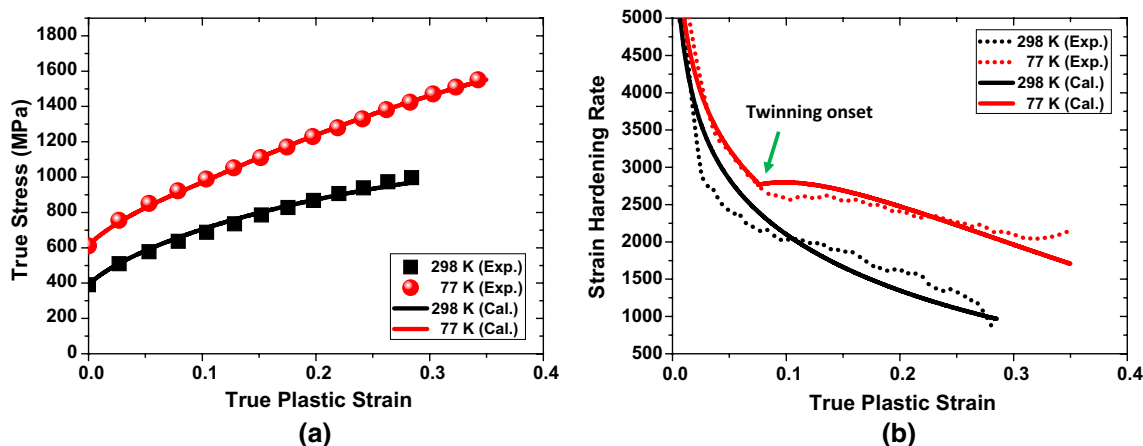


Fig. 7 a Stress–strain curves and b strain-hardening-rate curves obtained by experiments and simulations at room and cryogenic temperatures

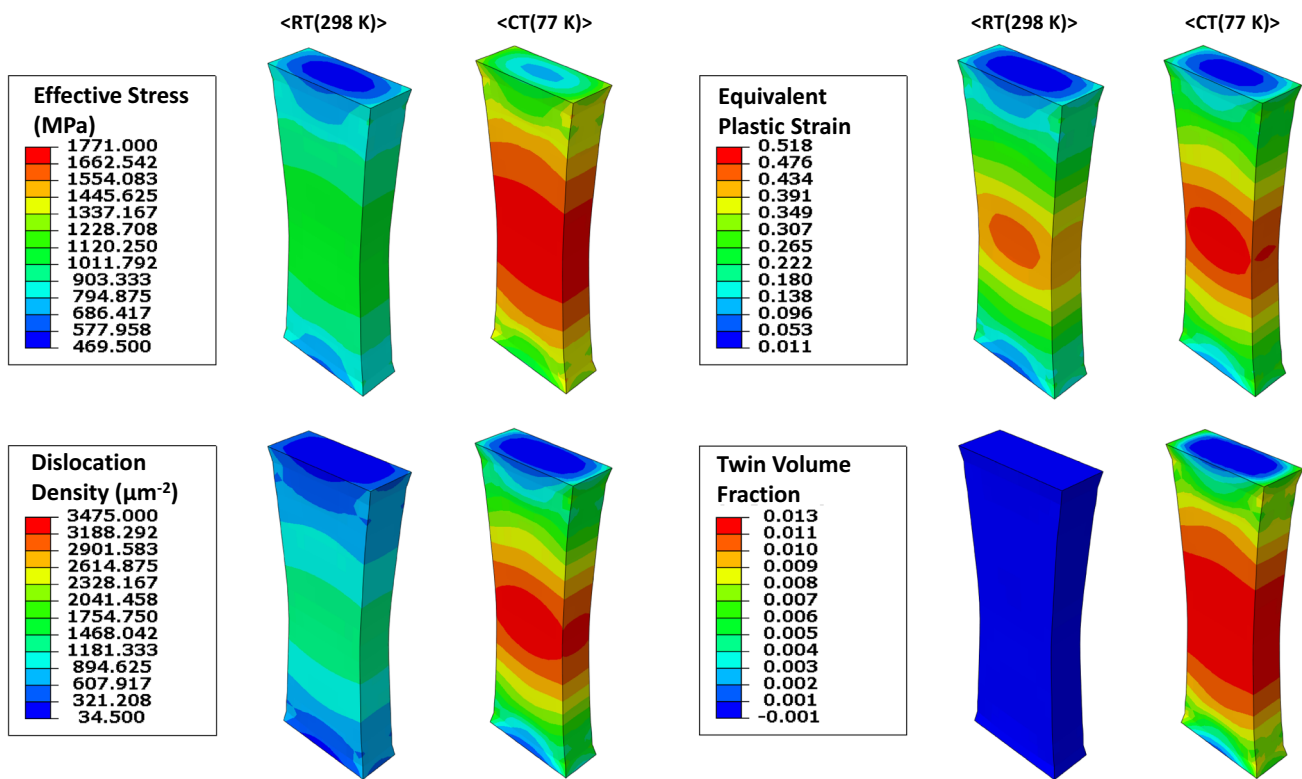


Fig. 8 Results of the finite element analyses: Effective stress, equivalent plastic strain, dislocation density, and twin volume fraction for room and cryogenic temperature

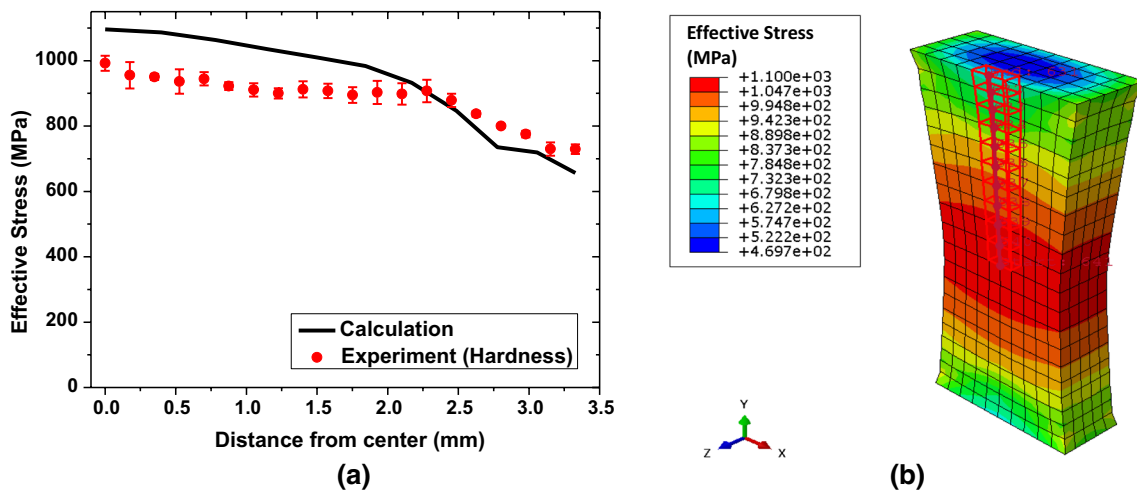


Fig. 9 a Line profile of effective stress and b distribution of effective stress (simulation result)

that the reason for the low hardness of the specimen in the central region is due to cracks or voids in the middle of the specimen. From these results, it can be confirmed that the plastic deformation behavior of the HEA at each temperature analyzed using the finite element method are in good agreement with the experimental results, and the validity of the simulation is assessed.

### 4 Conclusions

In the present study, an HEA for cryogenic applications was designed using thermodynamic calculations and the alloy was fabricated using casting and rolling methods. The alloy showed enhanced mechanical properties at

cryogenic temperature than at room temperature, verifying its suitability as a material for cryogenic environments. The deformation behavior of HEA was analyzed theoretically. The finite element analysis was carried out to understand the deformation mechanisms and the relationship between the microstructural characteristics and deformation behavior. The results of the simulation were verified by comparing them with the experimental results.

**Acknowledgements** This work was supported by the Future Material Discovery Program of the National Research Foundation of Korea (NRF) funded by the Ministry of Science, ICT and Future Planning (MSIP) of Korea (2016M3D1A1023384). In addition, this work was supported by the National Research Foundation of Korea (NRF) and Center for Women in Science, Engineering and Technology (WISSET) grant funded by the Ministry of Science and ICT (MSIT) under the team research program for female engineering students. SP acknowledges that this research was supported by Korea Research Fellowship program funded by the Ministry of Science, ICT and Future Planning through the National Research Foundation of Korea (2017H1D3A1A01013666).

## References

1. D.L. Gautier, K.J. Bird, R.R. Charpentier, A. Grantz, D.W. Houseknecht, T.R. Klett, T.E. Moore, J.K. Pitman, C.J. Schenk, J.H. Schuenemeyer, *Science* **324**, 1175 (2009)
2. N. Hong, *Res. Transp. Econ.* **35**, 50 (2012)
3. D.-H. Park, S.-W. Choi, J.-H. Kim, J.-M. Lee, *Cryogenics* **68**, 44 (2015)
4. W.S. Park, S.W. Yoo, M.H. Kim, J.M. Lee, *Mater. Des.* **31**, 3630 (2010)
5. B. Gludovatz, A. Hohenwarter, D. Catoor, E.H. Chang, E.P. George, R.O. Ritchie, *Science* **345**, 1153 (2014)
6. Y. Zhang, T.T. Zuo, Z. Tang, M.C. Gao, K.A. Dahmen, P.K. Liaw, Z.P. Lu, *Prog. Mater. Sci.* **61**, 1 (2014)
7. K.Y. Tsai, M.H. Tsai, J.W. Yeh, *Acta Mater.* **61**, 4887 (2013)
8. M.-H. Tsai, J.-W. Yeh, *Mater. Res. Lett.* **2**, 107 (2014)
9. V. Soare, D. Mitrica, I. Constantin, G. Popescu, I. Csaki, M. Tarcolea, I. Carcea, *Metall. Mater. Trans. A* **46A**, 1468 (2015)
10. T. Cao, J. Shang, J. Zhao, C. Cheng, R. Wang, H. Wang, *Mater. Lett.* **164**, 344 (2016)
11. Y.F. Ye, Q. Wang, J. Lu, C.T. Liu, Y. Yang, *Mater. Today* **19**, 349 (2016)
12. S. Praveen, H.S. Kim, *Adv. Eng. Mater.* **20**, 1700645 (2018)
13. B.H. Choe, H.S. Jang, H.S. Kim, J.U. Moon, *Korean J. Met. Mater.* **55**, 684 (2017)
14. M. Kang, J.W. Won, K.R. Lim, S.H. Park, S.M. Seo, Y.S. Na, *Korean J. Met. Mater.* **55**, 732 (2017)
15. B. Lee, B. Sundman, *TCFE2000: The Thermo-Calc Steels Database* (KTH, Stockholm, 1999)
16. K.-G. Chin, H.-J. Lee, J.-H. Kwak, J.-Y. Kang, B.-J. Lee, *J. Alloys Compd.* **505**, 217 (2010)
17. W.-M. Choi, S. Jung, Y.H. Jo, S. Lee, B.-J. Lee, *Met. Mater. Int.* **23**, 839 (2017)
18. N. Park, B.-J. Lee, N. Tsuji, *J. Alloys Compd.* **719**, 189 (2017)
19. M.J. Jang, D.-H. Ahn, J. Moon, J.W. Bae, D. Yim, J.-W. Yeh, Y. Estrin, H.S. Kim, *Mater. Res. Lett.* **5**, 350 (2017)
20. Y. Estrin, H. Mecking, *Acta Metall.* **32**, 57 (1984)
21. U.F. Kocks, H. Mecking, *Prog. Mater. Sci.* **48**, 171 (2003)
22. O. Bouaziz, N. Guelton, *Mater. Sci. Eng. A* **319–321**, 246 (2001)
23. O. Bouaziz, S. Allain, C.P. Scott, P. Cugy, D. Barbier, *Curr. Opin. Solid State Mater. Sci.* **15**, 141 (2011)
24. J.-H. Kang, T. Ingendahl, W. Bleck, *Mater. Des.* **90**, 340 (2016)
25. Y. Jo, S. Jung, W. Choi, S. Sohn, H. Kim, B. Lee, N. Kim, S. Lee, *Nat. Commun.* **8**, 1 (2017)
26. L. Zhang, M. Wen, M. Imade, S. Fukuyama, K. Yokogawa, *Acta Mater.* **56**, 3414 (2008)
27. C.-H. Hsu, M.-L. Chen, C.-J. Hu, *Mater. Sci. Eng. A* **444**, 339 (2007)
28. S.-H. Joo, H. Kato, M.J. Jang, J. Moon, C.W. Tsai, J.W. Yeh, H.S. Kim, *Mater. Sci. Eng. A* **689**, 122 (2017)
29. Z. Wu, C.M. Parish, H. Bei, *J. Alloys Compd.* **647**, 815 (2015)
30. W.H. Liu, Y. Wu, J.Y. He, T.G. Nieh, Z.P. Lu, *Scr. Mater.* **68**, 526 (2013)
31. M.J. Jang, S.-H. Joo, C.-W. Tsai, J.-W. Yeh, H.S. Kim, *Met. Mater. Int.* **22**, 982 (2016)
32. Y.-K. Lee, *Scr. Mater.* **66**, 1002 (2012)
33. G. Laplanche, A. Kostka, O. Horst, G. Eggeler, E. George, *Acta Mater.* **118**, 152 (2016)
34. E. Pavlina, C. Van Tyne, *J. Mater. Eng. Perform.* **17**, 888 (2008)